Progress In Electromagnetics Research M, Vol. 137, 45–55, 2026

(Received 30 December 2025, Accepted 26 January 2026, Scheduled 5 March 2026)

Optimized Low-Profile Coding Metasurface for Broadband and Wide-Angle RCS Reduction

Ke Wang[1, 2, *], Wei Li[3, *], Chao Zhang[3], Yizhao Zhou[1, 2], and Shijie Xie[1, 2]

[1] *School of Information Engineering, Jiangsu College of Engineering and Technology, Nantong, China*
[2] *Nantong Key Laboratory of Artificial Intelligence New Quality Technology*
Jiangsu College of Engineering and Technology, Nantong, China
[3] *State Key Laboratory of Millimeter Waves, Southeast University, Nanjing, China*

ABSTRACT: This study proposes a broadband, wide-angle metasurface for bistatic radar cross-section (RCS) reduction by integrating a low-profile bent-line unit design with an Adaptive Binary Particle Swarm Optimization algorithm enhanced by Array Pattern Synthesis (ABPSO-APS). The optimized metasurface achieves over 10 dB of bistatic RCS reduction across 8.4–21 GHz (86.7% fractional bandwidth), with a peak reduction of 22 dB, outperforming conventional checkerboard, genetic algorithm, and particle swarm optimization layouts by 22.82%, 15.27%, and 7.91%, respectively. The design also exhibits angular stability up to 30° and polarization insensitivity under both TE and TM incidences, while maintaining an ultrathin profile of only 0.1λ (where λ is the wavelength at the center frequency). These results demonstrate its strong potential as a compact and efficient solution for advanced electromagnetic stealth and radar signature control applications.

1. INTRODUCTION

Radar cross section (RCS) reduction is an important topic in the fields of national security and electromagnetic (EM) engineering, as it possesses considerable theoretical value and notable military relevance. A fundamental benefit lies in drastically reducing the observability of the target in radar detection, thereby dramatically improving the battlefield survivability of the modern military equipment. Conventional RCS reduction techniques focus on two basic approaches: optimization of the shape [1, 2] and implementation of radar-absorbing materials [3, 4]. Shape optimization is an efficient method for reducing the radar echo intensity by improving the geometric configuration of the target. Nevertheless, such modifications to the shape and structure can affect the maneuverability of the target. Radar-absorbing materials, designed to absorb EM waves through impedance matching, are typically thicker and more expensive. In recent years, advances in metasurface technology have revolutionized the field of radar stealth. This artificially designed EM material has demonstrated extraordinary EM wave modulation capabilities, including the ability to independently manipulate the amplitude, phase, and frequency properties of EM waves, thereby providing a completely new technological path to realize efficient scattered wave modulation [5–12]. Based on amplitude modulation, the metasurface converts the incident EM wave into thermal energy by means of a delicately designed resonant structure; however, its narrowband absorption characteristics have always been a constraint for practical applications. Therefore, several studies have introduced innovative designs, such as double concentric circle structures and multi-layer composite structures, which successfully expand the working bandwidth through the mechanism of multi-resonance coupling [13–16]. Regarding phase modulation, the mainstream techniques of scattered field steering, beam diffusion, and field cancellation exhibit distinctive features. The former realizes beam shifting by reconfiguring the phase distribution to reduce the RCS of the target [17–20]. In [17], a holographic metasurface was proposed to convert an incident EM wave into a surface wave to achieve an RCS reduction of more than 10 dB with 27% bandwidth. Optical transformation provides an efficient method of bending the incident EM wave along a given region, enabling an almost perfect stealth of the target [18–20]. The beam diffusion technique intelligently distributes the EM energy throughout space using phase-coding components [21–24]. In [21], a 3-bit coding metasurface was proposed to realize wideband RCS reduction at 6.9–14.5 GHz. By combining beam diffusion and absorption, a broadband metasurface is proposed to obtain 10 dB RCS reduction at 6.7–19.3 GHz [22]. Field cancellation, which utilizes 180° inverted cells to produce phase cancellation interference, reduces the RCS of the target [25–29]. The original technique was to combine a perfect electrical conductor (PEC) with an artificial magnetic conductor (AMC); however, restricted by the performance of the AMC unit cell, its 10 dB RCS reduction bandwidth is limited to 6.5% [25]. Recently, the employment of two polarization conversion metasurfaces (PCMs) with a phase difference of 180° has greatly expanded the operating bandwidth. The metasurface reported in [26] employs a slanted open-ring and cut-line resonator unit to extend the 10 dB RCS reduction relative bandwidth to 60%. The operating bandwidth of RCS reduction can be further improved by

---

* Corresponding authors: Ke Wang (wangke_nt@hotmail.com); Wei Li (liwei_seu@126.com).

doi:10.2528/PIERM25123003

Published by THE ELECTROMAGNETIC ACADEMY

designing multi-resonant PCMs [27–29]. Furthermore, broadband RCS reduction has been achieved by arranging a series of units with stable phase differences in a specific coding matrix through coding strategies and optimization algorithms [30–33]. In [30], researchers proposed an efficient wideband RCS reduction method using a checkerboard metasurface optimized via an ergodic algorithm. Subsequently, simulated annealing (SA), particle swarm optimization (PSO), and genetic algorithms (GA) were successively applied to optimize metasurface coding strategies [31–34]. Building on the foundation of broadband passive designs, the frontier of metasurface research is shifting toward reconfigurable intelligence. The incorporation of active components, such as PIN diodes, has enabled metasurfaces that no longer offer a single static response but can adaptively switch between dual modes (e.g., broadband RCS reduction and specular reflection) in real-time [35, 36]. However, optimizing both active and passive metasurface systems for RCS reduction presents substantial challenges, particularly in achieving effective control over the bistatic scattering characteristics, which remains underexplored.

In this study, a single-layer encoding metasurface for RCS reduction was designed, which has the advantages of thinness, broadband, wide angle, and polarization insensitivity. The metasurface employed a unique bent linear cell structure for efficient cross-polarization conversion. Meanwhile, to enhance the performance of the metasurface in bistatic RCS reduction, the adaptive binary particle swarm optimization (ABPSO) algorithm fused with the array pattern synthesis (APS) technique is applied to construct a loss function that includes bistatic RCS reduction, and ultimately, the optimal arrangement of the metasurface is realized. The RCS reduction performance of the metasurface with the checkerboard and other optimized algorithm arrangements are compared and analyzed, and the proposed metasurface has a more outstanding RCS reduction effect in the X, Ku, and K bands. The simulated and experimental results indicate that the metasurface has more than 10 dB of bistatic RCS reduction over a frequency of 8.4–21 GHz, and the maximum bistatic RCS reduction is improved by 6.7 dB. This performance is significantly superior to those achieved by the random, checkerboard, GA, and PSO arrangements. Moreover, the metasurface is insensitive to the polarization of the incident EM wave, and the performance of the metasurface at oblique incidence is essentially unchanged from that at normal incidence. The experimental and simulated results verified the reliability and effectiveness of the designed metasurface.

2. THEORETICAL ANALYSIS

To design a broadband low-scattering metasurface, it is necessary to study its working principles to provide a theoretical basis for the subsequent design and research. Assuming that the metasurface is composed of an $M \times N$ array of unit cells, according to electromagnetic theory [37], when a plane wave is incident on the metasurface, the resulting far-field electric field distribution can be expressed as:

$$\vec{E}_s(\theta,\varphi) = f(\theta,\varphi) \times AF(\theta,\varphi), \tag{1}$$

where $f(\theta,\varphi)$ denotes the element factor, and the array factor is as follows:

$$AF(\theta,\varphi) = \sum_{m=1}^{M}\sum_{n=1}^{N} R_{m,n} e^{-jk[(m-1/2)d_x\cos\varphi+(n-1/2)d_y\sin\varphi]\sin\theta}, \tag{2}$$

where $R_{m,n}$ represents the reflection coefficients of the arbitrary unit cell in the metasurface; θ and φ are the elevation and azimuth angles in any direction, respectively; and distances d_x and d_y are the intervals between the unit cells along the x- and y-axes, respectively. Because the electrical size of the coding unit cell is usually smaller than $4/\lambda$, the detailed information of the unit structure is diminished in the far-field region, meaning that the far-field scattering pattern of the entire metasurface is solely manipulated by $AF(\theta,\varphi)$.

Compared to a metallic flat plate of the same area, the RCS reduction of the metasurface can be expressed as

$$RCS_{reduction} = 20\log\left|\vec{E}_s(\theta,\varphi)/\vec{E}_i\right|, \tag{3}$$

where $\vec{E}_s(\theta,\varphi)$ represents the electric field of the metasurface at the angle θ and φ under an incident wave, and $\vec{E}_i$ represents the incident wave. The ratio of the scattered and incident fields is equal to the metasurface's reflection coefficient.

When the incident wave has normal incidence ($\theta = 0°$), Eq. (3) can be approximated

$$RCS_{reduction} = 20\log\left|\left(\sum_{m=1}^{M}\sum_{n=1}^{N} R_{m\cdot n}\right)/(M\times N)\right|, \tag{4}$$

which does not include edge effects. For a 1-bit coding metasurface, the amplitude and phase of the reflection of the cells have two distinct values. To maximize the value of Eq. (4), the reflection coefficients of two-cell structures should satisfy the following conditions:

$$R_{m\cdot n} = \left\{\begin{matrix} Ae^{j\varphi_0} \\ Ae^{j(\varphi_0+\pi)} \end{matrix}\right\}, \tag{5}$$

where A and φ_0 are the lattice reflection amplitude and phase coefficient, respectively. According to Eq. (5), to design a 1-bit metasurface, two types of unit cells with 0 and π phase responses are required to mimic the "0" and "1" elements, respectively. Simultaneously, the quantity ratios of the "0" and "1" elements were maintained approximately equal. Such a well-designed phase difference and quantity balance will lead to a perfect phase cancellation interference between the scattered waves of "0" and "1" elements in the far-field region, which realizes the effective regulation of the spatial distribution of EM wave energy. In practice, the phase response of the unit cell is influenced by the adjacent unit cells, which results in a deviation of the RCS reduction value from theory. In this case, the cell arrangement must be optimized to achieve a superior RCS reduction. Here, the optimal metasurface arrangement is

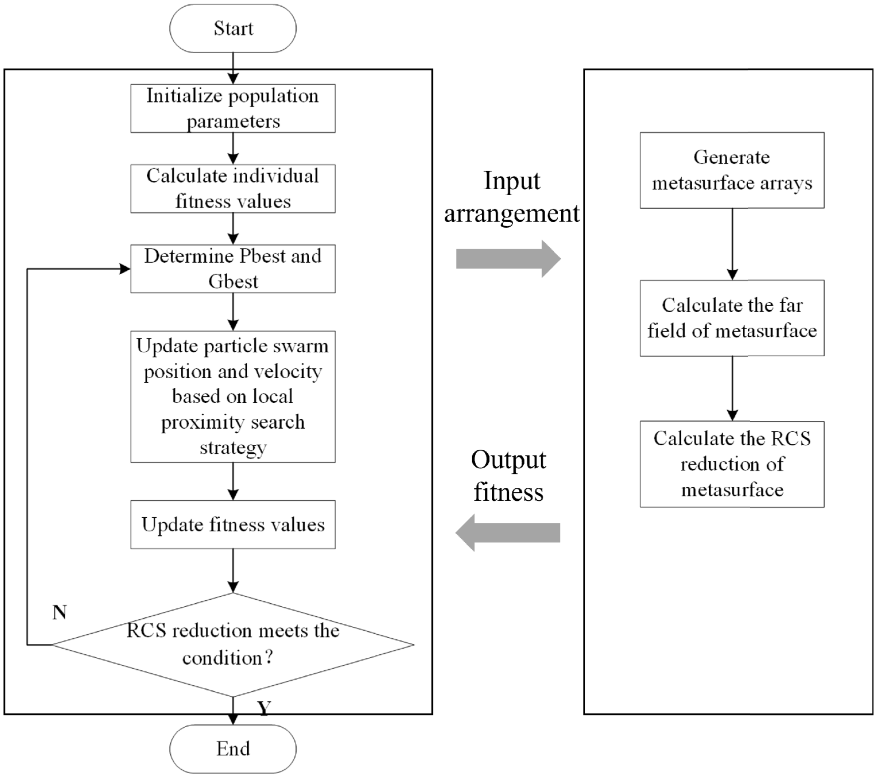

FIGURE 1. Flowchart of ABPSO-APS algorithm.

obtained through the implementation of the ABPSO-APS algorithm, where ABPSO represents an advanced evolutionary algorithm specifically designed for solving complex nonlinear optimization problems. To avoid the optimization process being trapped in local optimal solutions, adaptively adjustable weight factors based on the BPSO are introduced. A flowchart of the ABPSO-APS applied in the present study is shown in Fig. 1, where two modules are used to obtain the desired optimal design. The ABPSO module calculates the velocity values based on predefined inertia weight coefficients and decay rates. Then, the particles are subjected to selection, crossover, and mutation operations to produce the next generation population. The APS module was designed to calculate the peak values of the far-field scattering function, and these computational results were subsequently fed into the ABPSO module for performance evaluation. Accordingly, the fitness function implemented in this algorithmic framework is formally designated as:

$$\begin{aligned} \textit{fitness} &= \min\{\max[F(\theta,\varphi)]\}, \\ &\qquad \theta\in[0^\circ,180^\circ],\ \varphi\in[0^\circ,360^\circ]. \end{aligned} \tag{6}$$

3. STRUCTURE DESIGN

Figure 2 illustrates the schematic of the proposed 1-bit coding low-scattering metasurface, featuring a three-layer architecture: (i) a top-layer meandering copper resonator ($\sigma = 5.7\times 10^7$ S/m, thickness $=35\,\mu$m) designed for multi-resonance excitation, (ii) an FR4 dielectric with relative permittivity $\varepsilon_r = 4.3$ and $\tan\delta = 0.02$ (thickness $= 2$ mm), and (iii) a complete copper ground plane that guarantees high reflectivity. The physical dimensions of the proposed metasurface are presented in Table 1. This engineered structure achieves optimal scattering control owing to its precisely designed material composition and geometric configuration. The "1" element is obtained by rotating "0" element by 90° along the z-axis, as shown in Figs. 2(b) and 2(c). In Computer Simulation Technology (CST) Microwave Studio, the unit cell was numerically simulated with Floquet port excitation along the z-axis. Periodic boundary conditions were applied along the x- and y-planes to emulate an infinite array, while open boundary conditions were set along the z-axis to simulate an unbounded environment.

TABLE 1. Physical dimensions of the proposed metasurface (Unit: mm).

a	d	L	w_1	w_2
7	0.5	2	0.55	0.3

As illustrated in Fig. 3, the reflection coefficients of Cells 0 and 1 under normal incidence exhibit multiple resonances, broadening the effective bandwidth. The reflection coefficient magnitudes of both unit cells exceed -1.5 dB from 8.6 to 21 GHz, while their phase difference (indicated by the shaded region) remains close to 180°, thereby satisfying the conditions of Eq. (4). Together with an optimized unit cell arrangement, these properties pave the way for an effective broadband RCS reduction.

Figure 4 shows the curves of the magnitude of the reflection coefficient versus frequency for different parameters. As the spacing d and length L increase, the reflection coefficient

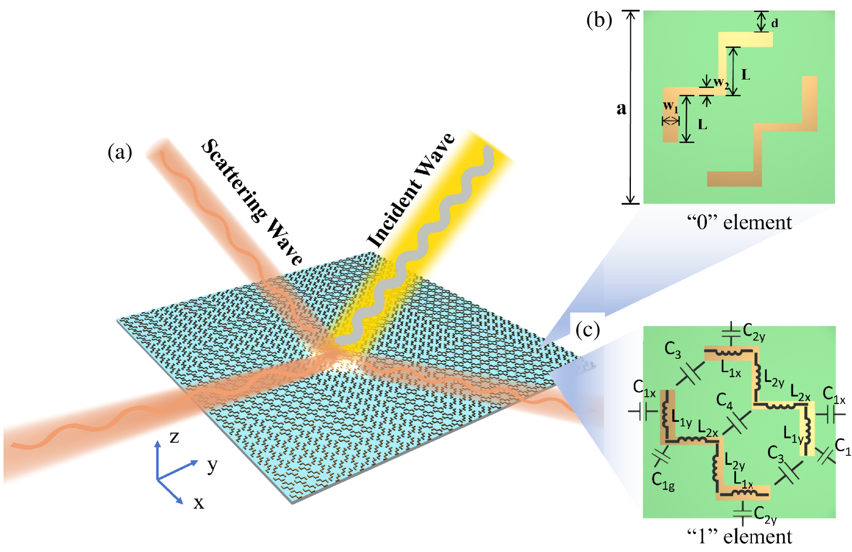

FIGURE 2. (a) Perspective view of the metasurface. (b) Top view of the "0" element. (c) Top view of the "1" element.

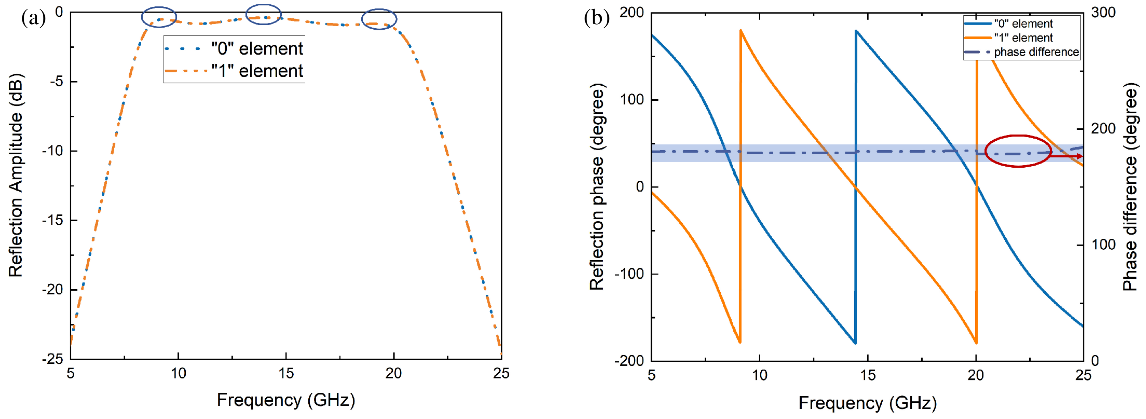

FIGURE 3. Reflection coefficients of "0" and "1" elements versus frequency under normal TE polarized EM incident waves: (a) Magnitude reflection coefficient. (b) Phase reflection coefficients of the '0' element versus the '1' element.

curve shifts toward lower frequencies, and its magnitude decreases. The reflection coefficient is not highly sensitive to width w_1; as w_1 increases, the magnitude decreases slightly. In contrast, as width w_2 increases, the reflection coefficient curve shifts toward higher frequencies, while the magnitude also decreases. Based on a comprehensive consideration of both bandwidth and reflection amplitude, the parameters summarized in Table 1 were determined.

To further analyze the performance of the proposed metasurface unit cell, we modeled it using an equivalent circuit representation. When an x-polarized electromagnetic wave interacts with a unit cell, it induces a current along the x-axis. In this equivalent circuit, capacitor C_{1x} originates from the capacitance between two adjacent unit cells; the metal meander line is modeled as inductors L_1' and L_2'; the capacitance between the metal meander lines is represented as C_2'; and the capacitance between the metal patch and ground plane is denoted as C_1'. A simplified version of this equivalent circuit is illustrated in Fig. 5, and its simulation is performed using Keysight ADS, with the corresponding optimized component values provided in the figure. Based on the optimized parameters, the reflection coefficients of the two equivalent circuits were calculated, as shown in Fig. 6. The observed discrepancies arise because the advanced design system (ADS) simulation relies solely on the Floquet mode analysis, whereas the CST simulation provides a more comprehensive solution by incorporating all coupling effects [38].

Figure 7 shows the surface current distribution of the unit structure at three resonant frequencies: 9.1 GHz, 14.1 GHz, and 19.6 GHz. The current flow directions, indicated by the vector arrows, reveal the distinct resonance mechanisms. At 9.1 GHz (Fig. 4(a)), the induced current on the top metal layer flows along the diagonal from the upper left to the lower right (J_1), whereas the current on the bottom metal layer follows the opposite diagonal direction (J_2). This antiparallel current distribution confirms that the structure operates in magnetic resonance mode at this frequency. A similar magnetic resonance was observed at 14.1 GHz (Fig. 4(b)), although with modified

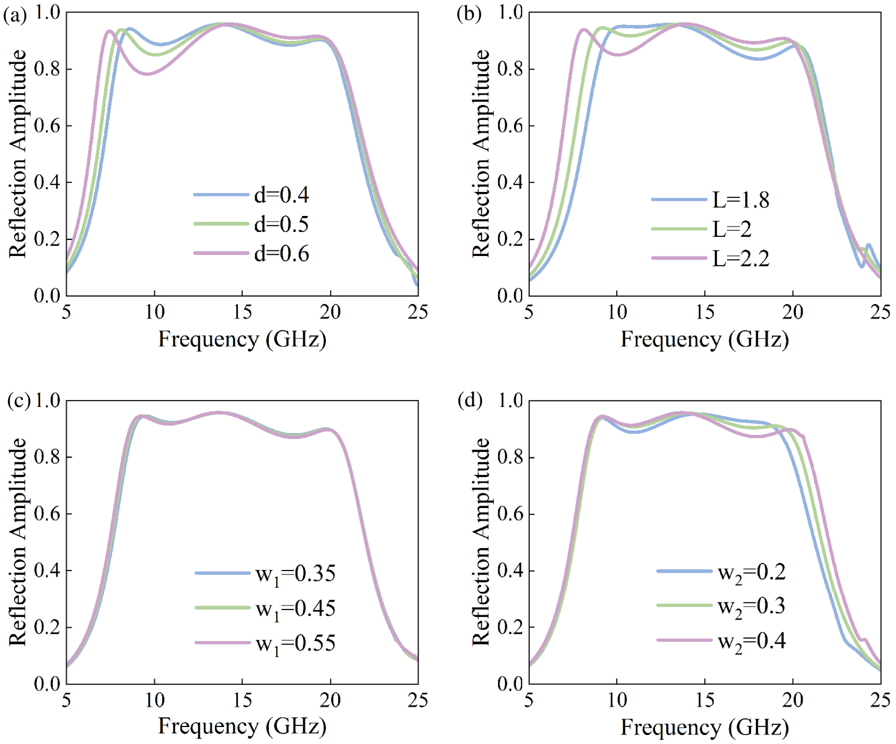

FIGURE 4. The reflection amplitudes of the element under different geometry parameters: (a) versus d, (b) versus L, (c) versus w_1, and (d) versus w_2.

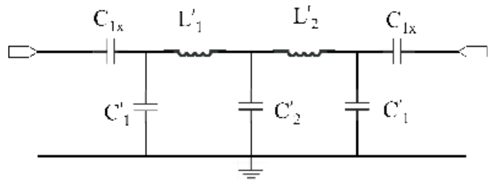

FIGURE 5. Equivalent circuit of the unit cell. $C_{1x} = 0.047\,\text{pF}$, $C'_1 = 0.029\,\text{pF}$, $L'_1 = L'_2 = 1.79\,\text{nH}$, $C'_2 = 0.012\,\text{pF}$.

current path densities (J_1) and (J_2). In contrast, at 19.6 GHz (Fig. 4(c)), the induced currents on both the top (J_1) and bottom surfaces (J_2) aligned in the same direction, indicating an electrical resonance mode. This behavior resembles cut-wire resonator characteristics, with currents primarily concentrated along the central axis of the structure. The coexistence of these multiple resonant modes enables broadband performance. By optimizing the structural parameters (Table 1), the individual resonant modes can be effectively coupled, thereby achieving a continuous and wide operating bandwidth.

4. SIMULATIONS AND MEASUREMENT RESULTS

In the ABPSO algorithm, the inertia weight is dynamically adjusted, and the specific formulation is expressed as follows:

$$\omega(t) = \exp^{-\left(\frac{bt}{T}\right)^b}, \tag{7}$$

where T is the maximum number of iterations, and b is a predetermined constant.

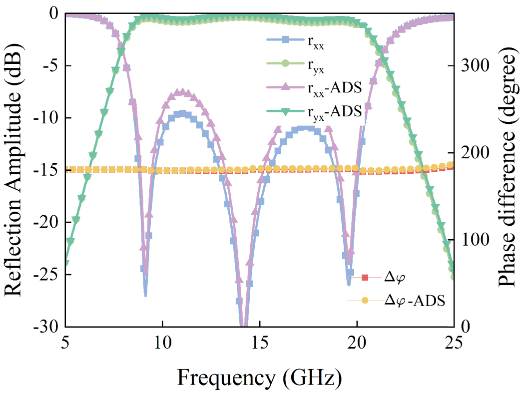

FIGURE 6. Reflection coefficients simulated by ADS and CST.

The formulation of the adaptive position update strategy is as follows:

$$\begin{aligned} V_i(t+1) = {} & \omega(t)V_i(t+1) + c_1 \times rand_1 \times (Pbest(t) - X_i(t)) \\ & + c_2 \times rand_2 \times (Gbest(t) - X_i(t)) \end{aligned} \tag{8}$$

$$X_i(t+1) = \left\{ \begin{array}{l} \omega(t)X_i(t) + (1-\omega(t))V_i(t+1) \\ +Gbest(t) \quad \text{when } p_i > rand_3 \\ X_i(t) + V_i(t+1) \quad \text{otherwise} \end{array} \right\}, \tag{9}$$

$$p_i = \frac{\exp\left(fitness(X_i(t))\right)}{\frac{1}{N}\exp\left(\sum_{i=1}^{N} fitness(X_i(t))\right)} \tag{10}$$

where $V(t)$ represents the particle velocity; p_i denotes the ratio of the particle's current fitness to the average population fitness; c_1 and c_2 are the acceleration constants; $rand_1$ and $rand_2$

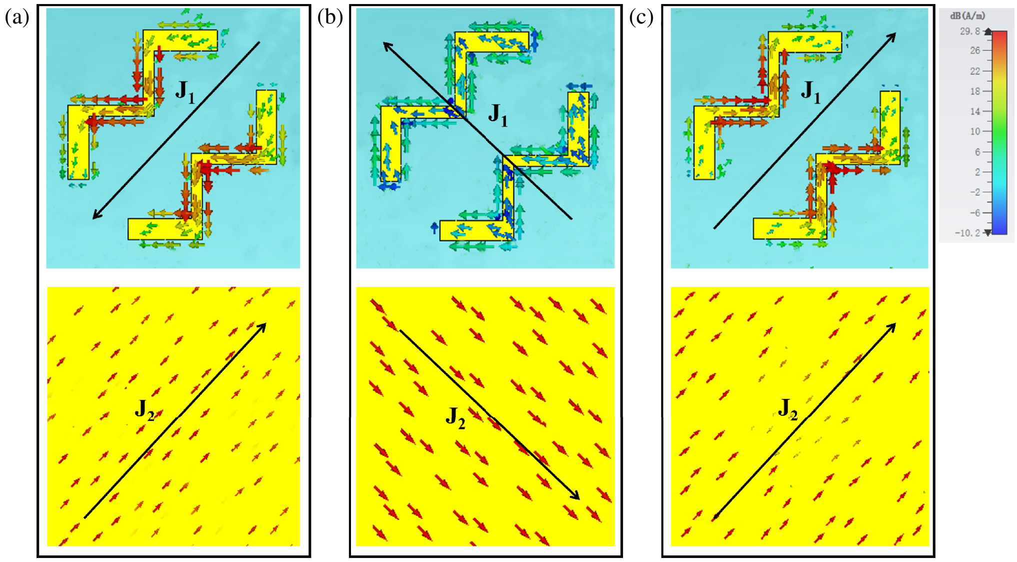

FIGURE 7. The top layer and ground plane surface current distributions of the proposed metasurface at three resonant frequencies: (a) 9.1 GHz, (b) 14.1 GHz, (c) 19.6 GHz.

Algorithm 1 ABPSO

```
Given: Reflected phases of units;
Return: Arrangement of metasurface;
Initialization parameters;
Randomly initialize position $X_i$;
Evaluate the initial fitness of $X_i$ (calculated the RCS reduction by APS algorithm);
for i = 1; i <= M do
    for j = 1; j <= N do
        Update the weight according to eq. (7);
        Update the position according to eq. (8) and eq. (9);
        Evaluate the fitness of $X_i$ according to eq. (6);
        if fitness of $X_i$ improves the solution then
            Update the parameters according to eq. (7), eq. (8) and eq. (9);
        else
            Maintain the parameters;
        end if
    end for
end for
```

are random numbers between 0 and 1. An estimated value is obtained in each iteration to adjust the strategy. *Pbest(t)* denotes the individual best position, and *Gbest(t)* denotes the global best position. If $p_i < \mathit{rand}_3$, the fitness of particle i is lower than the average fitness, meaning that its performance is superior to the population average. To enhance its global exploration capability, the position of particle i is updated using strategy $\mathbf{X} = \mathbf{X}+\mathbf{V}$. If $p_i > \mathit{rand}_3$, and the fitness of particle i is higher than the average fitness, implying that its performance is inferior to the population average. In this case, the local exploitation capability of particle i is enhanced. The position of particle i was updated using the strategy $\mathbf{X} = \mathbf{w}\mathbf{X} + (1 - \mathbf{w})\mathbf{V}$. The ABPSO-APS optimization was configured with the following parameters: maximum iteration count of 300, particle dimension of 100 (corresponding to the 10×10 metasurface design space), and constants $b = 0.3$, $c_1 = 1.5$, and $c_2 = 1.5$. The complete procedure is outlined in the pseudo-code provided in Algorithm 1. The computational complexity of the proposed algorithm is $O(N \times M)$, where N and M denote the population size and the number of iterations, respectively. All simulations were performed on a workstation equipped with an i7 processor (3.0 GHz), 32 GB RAM, and a 64-bit operating system. The average runtime recorded on this system is approximately 1.5 hours.

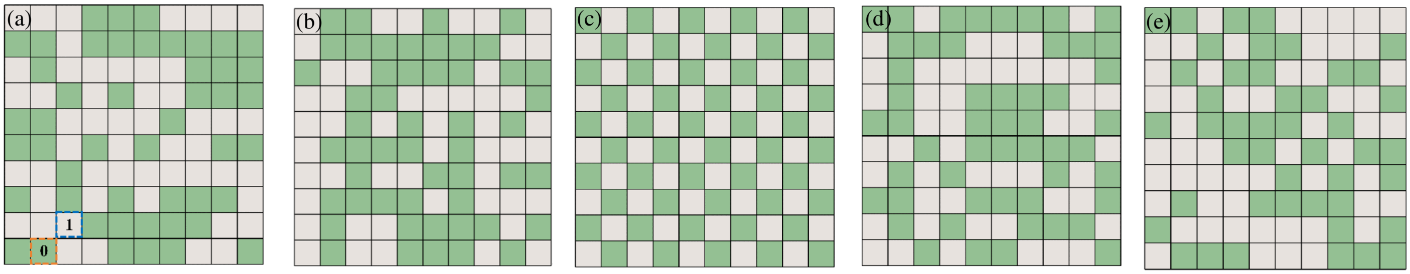

FIGURE 8. Different coding matrices: (a) proposed arrangement, (b) random arrangement, (c) checkerboard arrangement, (d) GA arrangement, (e) PSO arrangement.

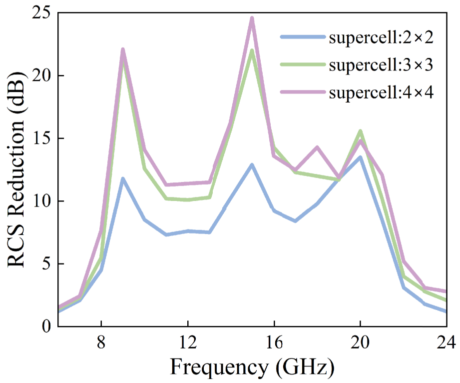

FIGURE 9. RCS reduction for different supercell configurations.

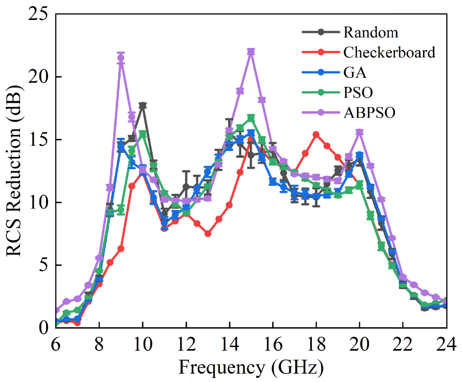

FIGURE 10. Simulated bistatic RCS reduction for metasurfaces with different coding sequences under normally incident TE-polarized waves. The error bars indicate the standard deviation across five independent optimization runs.

The resulting low-scattering metasurface cell arrangement obtained through this optimization process is presented in Fig. 8(a). To compare the RCS reduction performance, the metasurface layouts were optimized using a random pattern [28], checkerboard pattern [26], genetic algorithm (GA) [31], and particle swarm optimization (PSO) [32], all based on the same unit cell structure. The corresponding unit cell distribution diagrams for the random, checkerboard, GA-optimized, and PSO-optimized layouts are shown in Figs. 8(b), 8(c), 8(d), and 8(e), respectively. Full-wave simulations were conducted to evaluate the RCS reduction performance of metasurfaces. To satisfy the periodic boundary condition in simulations, each "1/0"-coded element was expanded into a supercell comprising identical unit cells to achieve the required phase response. To evaluate the influence of supercell size on the simulation outcomes, three configurations with fundamental unit dimensions of 2×2, 3×3, and 4×4 were designed and compared in terms of their RCS reduction performance. Fig. 9 compares the RCS reduction under the same coding sequence (as shown in Fig. 8(a)) for these different supercell sizes. The results indicate that RCS reduction generally improves with an increase in supercell dimension. However, when comparing the 4×4 supercell to the 3×3 configuration, further enhancement in RCS reduction becomes marginal, with performance stabilizing and showing little appreciable change. Based on a balance among the overall metasurface size, achievable performance, and practical measurement feasibility, the 3×3 supercell was selected as the optimal design choice.

A comparison of the RCS performance achieved by the randomly, chessboard, GA, PSO, and ABPSO-APS optimized metasurfaces for normally incident waves is presented in Fig. 10. To ensure an objective and impartial evaluation of each algorithm, we executed five independent runs for each method in our simulation experiments, maintaining a consistent set of algorithm parameters across all runs. Compared to the other three optimization methods, the ABPSO-APS algorithm achieves greater RCS reduction with an extended bandwidth. Over the entire frequency band of 8.4 to 21 GHz, an RCS reduction of more than 10 dB is attained, reaching a maximum of 22 dB at 14.5 GHz. The overall improvement in the RCS reduction performance, denoted by r, can be calculated using Eq. (11) [39]:

$$r = \frac{1}{n}\sum_{i=1}^{n}\frac{RCS_x(i) - RCS_{ABPSO}(i)}{RCS_x(i)}, \tag{11}$$

where $RCS_x(i)$ represents the bistatic RCS value at frequency point i obtained using the phase distributions optimized by the chessboard, GA, or PSO methods, and $RCS_{ABPSO}(i)$ denotes the bistatic RCS value at frequency point i achieved with the ABPSO-APS optimized phase distribution. Here, frequency point i ranges from 8 to 21 GHz with a sampling interval of 0.1 GHz. The overall performance improvement was determined by averaging the values calculated using Eq. (11) across these runs. Based on the calculation, the overall RCS reduction improvement is 22.82% compared to the checkerboard layout, 15.27% compared to the GA method, and 7.91% compared to

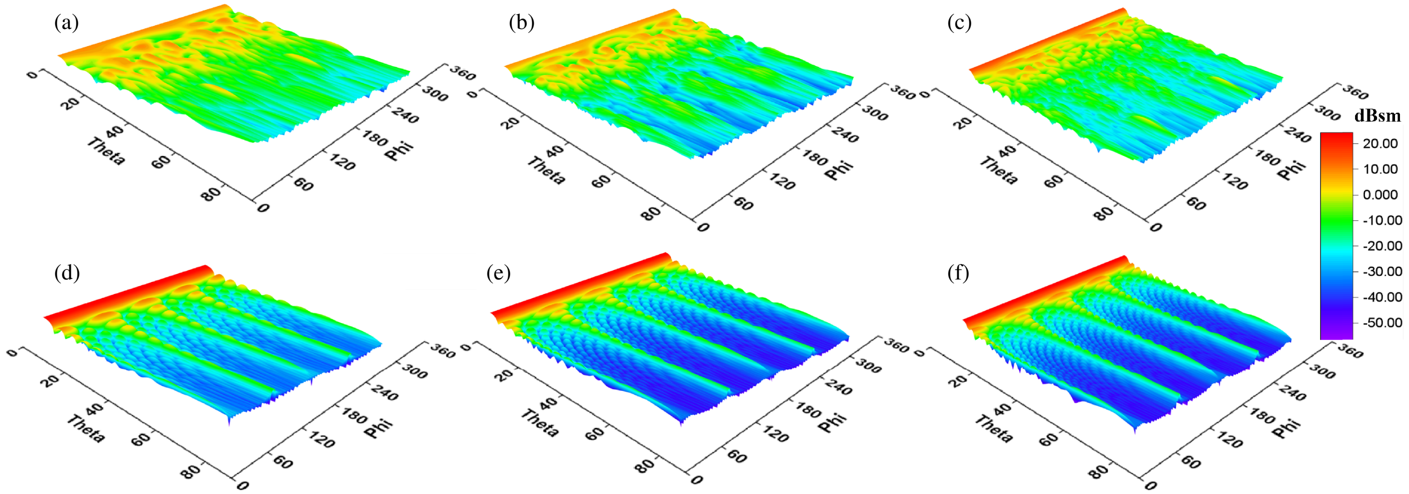

FIGURE 11. 2D far-field radiation pattern under normal incidence, (a) metasurface at 10 GHz, (b) metasurface at 15 GHz, (c) metasurface at 20 GHz, (d) metallic plate at 10 GHz, (e) metallic plate at 15 GHz, (f) metallic plate at 20 GHz.

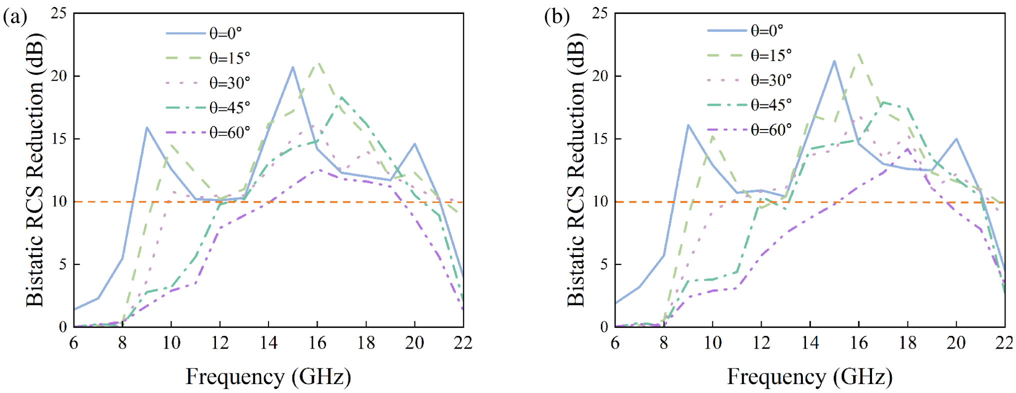

FIGURE 12. The simulated bistatic RCS reduction results of the proposed metasurface under different polarized incident waves. (a) TE waves. (b) TM waves.

the standard PSO algorithm. These metrics clearly demonstrate the exceptional capability of the optimized design for broadband scattering suppression, maintaining a consistent RCS reduction throughout the operational bandwidth while achieving higher peak reduction values.

To further investigate the RCS reduction performance of the proposed metasurface, two-dimensional far-field radiation patterns were simulated and are shown in Fig. 11. The scattering characteristics of the metasurface were comprehensively compared with those of a metal plate with equivalent dimensions at three representative frequencies: 10 GHz, 15 GHz, and 20 GHz. In accordance with the principle of energy conservation, the strategic redistribution of scattered energy to the side lobes effectively suppresses the main-lobe intensity, thereby achieving a significant RCS reduction in the specular direction. The orientation patterns clearly demonstrate that while the metal plate maintains a strong main lobe in the vertical direction ($\theta = 0°$) across the entire frequency band, the metasurface effectively manipulates the scattering profile to produce more uniform far-field radiation. The optimized design not only achieves broadband RCS reduction but also enables a dynamic control of the scattered field distribution. The bistatic RCS reduction performance of the proposed metasurface was quantitatively evaluated through numerical simulations of the TE and TM incident waves at various incidence angles, as illustrated in Fig. 12. Under normal incidence conditions, the metasurface exhibits notable scattering suppression capabilities, achieving bistatic RCS reductions exceeding 10 dB across an operational bandwidth spanning from 8.4 to 21 GHz, which is equivalent to an 85.7% relative bandwidth. While oblique incidence leads to a gradual degradation in the RCS reduction performance, the structure maintains its broadband effectiveness when the incident angle is less than 30°. As the incidence angle increased to 15°, the 10 dB RCS reduction bandwidth exhibited no significant variation. When the incidence angle was further increased to 30°, the 10 dB RCS reduction bandwidth became 9–21 GHz (80% relative bandwidth). Upon increasing the incidence angle to 45°, the 10 dB RCS reduction bandwidth decreased, narrowing to 12–21 GHz (54.5% relative bandwidth). Distinct frequency-dependent behavior emerges where the peak reduction shifts toward higher frequencies with increasing incidence angles. Notably, the maximum RCS reduction of 18 dB persisted even at oblique incidences up to 45°. However, the 10 dB RCS reduction bandwidth deteriorates significantly as

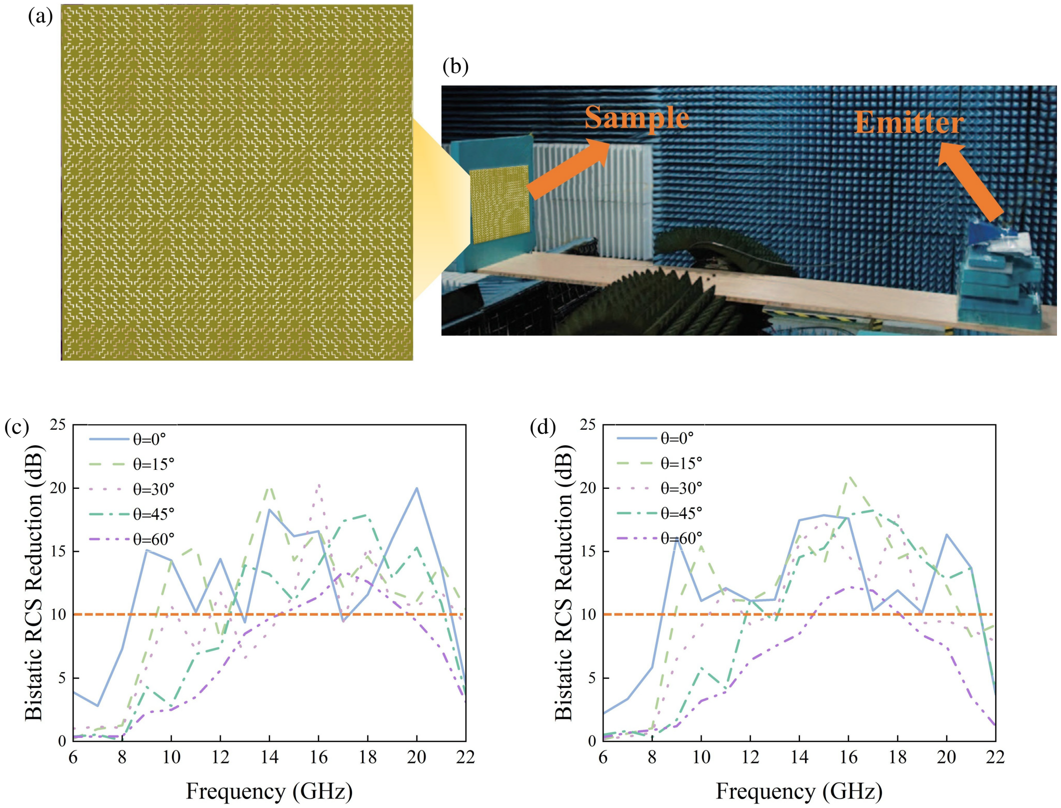

FIGURE 13. Experimental verification of the proposed metasurface. (a) Photographs of the fabricated sample. (b) The experimental setup. (c) Measured bistatic RCS reduction results under TE waves. (d) Measured bistatic RCS reduction results under TM waves.

the incident angle increases to 60°. These findings collectively demonstrate that the proposed metasurface provides consistent bistatic scattering suppression while preserving broadband performance across a wide angular range, making it ideal for practical applications that require wide-angle radar stealth.

To experimentally verify the concept proposed in this work, a sample encoded with a sequence (Fig. 8(a)) was fabricated using the standard printed circuit board (PCB) process on an FR4 substrate, as shown in Fig. 13(a). The fabricated sample consisted of a 10×10 array of coding units with a supercell size of 3×3, yielding a total physical dimension of $210 \times 210\,\mathrm{mm}^2$, and all geometric parameters were maintained identical to those used in the numerical simulations. Measurements were conducted in a standard microwave chamber using the experimental setup shown in Fig. 13(b). The distance between the antenna and metasurface was 3 m, which satisfies the far-field condition $R > 2D^2/\lambda$, where D is the maximum aperture dimension of the antenna, and λ is the wavelength at the highest operating frequency. The receiving antenna mounting platform performed automated 360° rotation in the horizontal plane with 0.1° angular resolution during testing, enabling comprehensive characterization of the 2D far-field scattering patterns. Fig. 13(c) and Fig. 13(d) present the measured bistatic RCS reduction performance for both TE and TM polarizations, showing that under normal incidence, the fabricated sample demonstrates more than 10 dB RCS reduction across 8.4–20.8 GHz with agreement to full-wave simulations. The polarization-insensitive nature of the design was confirmed by the consistent performance under both TE and TM incident waves. For oblique incidence up to 60°, the measured results maintain good correlation with the simulated trends, despite minor discrepancies attributable to fabrication tolerances in PCB manufacturing, alignment uncertainties in the measurement system, and slight variations in substrate dielectric properties. The observed angular stability in the measurements validates the robustness of our phase optimization approach. While current facility limitations prevent full 3D pattern measurements, the obtained 2D results sufficiently demonstrate the effectiveness of our design methodology for achieving broadband bistatic RCS reduction. The close agreement between the experimental and simulated results confirms both the validity of our numerical models and the practical feasibility of the proposed metasurface design, particularly in terms of maintaining an effective scattering suppression across wide bandwidths and varying incidence angles.

Table 2 presents a comparative analysis of the proposed method and recent studies. The results clearly indicate that the metasurface proposed in this study demonstrates significant advantages for achieving broadband RCS reduction. It is noted that Ref. [32] employed a thicker dielectric substrate to extend the operational bandwidth, which is disadvantageous for system integration. In contrast, the present study achieves bistatic RCS reduction from 8.4 to 21 GHz (86.7% fractional bandwidth) with an ultrathin profile of only 0.1λ (where λ is the wavelength at the center frequency), while maintaining angular stability up to 30° and polarization-insensitive performance. It is also important to discuss the inherent trade-off between spe-

TABLE 2. Comparison with previous works.

Reference	Thickness (d/λ^*)	Unit Size (L/λ^*)	Metasurface arrangement	10 dB monostatic RCS reduction bandwidth	10 dB bistatic RCS reduction bandwidth	Angular Stability (°)	Polarization -insensitive
[26]	0.08	0.28	Checkerboard	8.1 to 14.6 GHz/57.3%	-	-	yes
[28]	0.12	0.37	Random	7.2–17.2 GHz/82.0%	7.2–17.2 GHz/82.0%	30	yes
[30]	0.06	0.11	EA	5.57–7.37 GHz/27.8%	-	45	-
[31]	0.05	0.27	GA	6.94–9.23 GHz/28.3%	-	40	yes
[32]	0.24	0.34	PSO	4–10.4 GHz/88.8%	-	-	-
[35]	0.12	0.45	Checkerboard	8.7–14.8 GHz/51.4%	-	30	yes
[36]	0.14	0.51	Random	10.8–23.2 GHz/72.9%	-	-	yes
This work	0.1	0.34	ABPSO	8.1–21 GHz/88.7%	8.4–21 GHz/86.7%	30	yes

Abbreviations: EA, ergodic algorithm; λ^*, wavelength of central operating frequency.

cialized broadband performance and multifunctional reconfigurability. For instance, reconfigurable designs such as [35] offer additional capabilities like dynamic polarization conversion and beam steering, but typically at the expense of narrower RCS reduction bandwidth (51.4% in this case) and increased design complexity due to integrated active components. In summary, the coding-optimized metasurface developed in this study exhibits a substantially broader operational bandwidth, demonstrating its strong potential for practical applications.

5. CONCLUSION

In summary, an optimized design method for the phase distribution of a metasurface based on the ABPSO-APS algorithm is proposed to efficiently achieve broadband bistatic RCS reduction. Using this optimization approach, we successfully designed a polarization-insensitive metasurface exhibiting broadband performance from 8.4 to 21 GHz. The full-wave simulation and experimental measurements demonstrate that our optimized metasurface achieves a remarkable 22.82% improvement in bistatic RCS reduction compared with conventional design methods, consistently delivering a reduction of over 10 dB across the entire operational bandwidth. The methodology addresses existing limitations in the computational efficiency and performance of RCS-reducing metasurfaces. These results suggest potential applications in large-scale array designs, where the technique can offer improved performance with reduced computational requirements. Furthermore, the findings contribute to ongoing research on EM scattering control and metasurface optimization.

ACKNOWLEDGEMENT

This study was supported by the National Natural Science Foundation of China (62201136), the Research Foundation of Science and Technology on Antenna and Microwave Laboratory (6142402220304), Jiangsu Province Young Teachers Enterprise Practice Program (2025QYSJ104), and the Natural Science Foundation of Jiangsu College of Engineering and Technology (JSGYZRJJYB-07).

REFERENCES

[1] Muniyasamy, A. and K. Rajakani, "UWB radar cross section reduction in a compact antipodal Vivaldi antenna," *AEU — International Journal of Electronics and Communications*, Vol. 99, 369–375, 2019.

[2] Zhang, K., R. Tan, Z. H. Jiang, Y. Huang, L. Tang, and W. Hong, "A compact, ultrawideband dual-polarized Vivaldi antenna with radar cross section reduction," *IEEE Antennas and Wireless Propagation Letters*, Vol. 21, No. 7, 1323–1327, 2022.

[3] Pozar, D. M., "RCS reduction for a microstrip antenna using a normally biased ferrite substrate," *IEEE Microwave and Guided Wave Letters*, Vol. 2, No. 5, 196–198, 1992.

[4] Kumar, D. and P. K. S. Pourush, "Circular patch microstrip array antenna on NiCoAl ferrite substrate in C-band," *Journal of Magnetism and Magnetic Materials*, Vol. 322, No. 9-12, 1635–1638, 2010.

[5] Yu, N., P. Genevet, M. A. Kats, F. Aieta, J.-P. Tetienne, F. Capasso, and Z. Gaburro, "Light propagation with phase discontinuities: Generalized laws of reflection and refraction," *Science*, Vol. 334, No. 6054, 333–337, 2011.

[6] Cui, T. J., M. Q. Qi, X. Wan, J. Zhao, and Q. Cheng, "Coding metamaterials, digital metamaterials and programmable metamaterials," *Light: Science & Applications*, Vol. 3, No. 10, e218, 2014.

[7] Huang, C., C. Zhang, J. Yang, B. Sun, B. Zhao, and X. Luo, "Reconfigurable metasurface for multifunctional control of electromagnetic waves," *Advanced Optical Materials*, Vol. 5, No. 22, 1700485, 2017.

[8] Galiffi, E., P. A. Huidobro, and J. B. Pendry, "Broadband nonreciprocal amplification in luminal metamaterials," *Physical Review Letters*, Vol. 123, No. 20, 206101, 2019.

[9] Li, J., P. Yu, S. Zhang, and N. Liu, "Electrically-controlled digital metasurface device for light projection displays," *Nature Communications*, Vol. 11, No. 1, 3574, 2020.

[10] Kim, G., Y. Kim, J. Yun, S.-W. Moon, S. Kim, J. Kim, J. Park, T. Badloe, I. Kim, and J. Rho, "Metasurface-driven full-space structured light for three-dimensional imaging," *Nature Communications*, Vol. 13, No. 1, 5920, 2022.

[11] Zheng, X., J. Lin, Z. Wang, H. Zhou, Q. He, and L. Zhou, "Manipulating light transmission and absorption via an achromatic reflectionless metasurface," *PhotoniX*, Vol. 4, No. 1, 3, 2023.

[12] Gao, C., T. Lai, L. Peng, X. Zhang, Z. Huang, Z. Wang, X. Pang, S. Zhao, and D. Ye, "Multifunctional intelligent reconfigurable metasurface," *ACS Applied Materials & Interfaces*, Vol. 16, No. 41, 55 675–55 683, 2024.

[13] Sambhav, S., J. Ghosh, and A. K. Singh, "Ultra-wideband polarization insensitive thin absorber based on resistive concentric circular rings," *IEEE Transactions on Electromagnetic Compatibility*, Vol. 63, No. 5, 1333–1340, 2021.

[14] Hannan, S., M. T. Islam, S. H. A. Almalki, M. R. I. Faruque, M. S. M, and M. S. Islam, "Rotational symmetry engineered, polarization and incident angle-insensitive, perfect metamaterial absorber for X and Ku band wireless applications," *Scientific Reports*, Vol. 12, No. 1, 3740, 2022.

[15] Hossain, M. B., M. R. I. Faruque, S. Abdullah, M. T. Islam, and K. S. Al-Mugren, "A coding based metasurface absorber with triple circular ring resonator for broadband RCS reduction and high EMI shielding effectiveness," *Results in Engineering*, Vol. 21, 101791, 2024.

[16] Lin, B., W. Huang, J. Guo, Z. Wang, K. Si, and H. Ye, "An absorptive coding metasurface for ultra-wideband radar cross-section reduction," *Scientific Reports*, Vol. 14, No. 1, 12397, 2024.

[17] Azizi, Y., M. Soleimani, and S. H. Sedighy, "Low cost, simple and broad band radar cross section reduction by modulated and holography metasurfaces," *Journal of Physics D: Applied Physics*, Vol. 52, No. 43, 435003, 2019.

[18] Schurig, D., J. J. Mock, B. J. Justice, S. A. Cummer, J. B. Pendry, A. F. Starr, and D. R. Smith, "Metamaterial electromagnetic cloak at microwave frequencies," *Science*, Vol. 314, No. 5801, 977–980, 2006.

[19] McCall, M., "Transformation optics and cloaking," *Contemporary Physics*, Vol. 54, No. 6, 273–286, 2013.

[20] Kishimoto, N., K. Izui, S. Nishiwaki, and T. Yamada, "Optimal design of electromagnetic cloaks with multiple dielectric materials by topology optimization," *Applied Physics Letters*, Vol. 110, No. 20, 201104, 2017.

[21] Gao, H., X. Huang, X. Ma, X. Li, L. Guo, and H. Yang, "An ultra-wideband coding polarizer for beam control and RCS reduction," *Frontiers of Physics*, Vol. 18, No. 4, 42301, 2023.

[22] Zhou, X., H. Yang, J. Jin, L. Guo, Y. Li, H. Cheng, Y. Fu, and Y. Dai, "A low-profile coding metasurface for broadband radar cross section reduction via beam diffusion and absorption," *Physica Scripta*, Vol. 99, No. 4, 045522, 2024.

[23] Ali, L., Q. Li, T. A. Khan, J. Yi, and X. Chen, "Wideband RCS reduction using coding diffusion metasurface," *Materials*, Vol. 12, No. 17, 2708, 2019.

[24] Taher Al-Nuaimi, M. K., W. G. Whittow, G.-L. Huang, R.-S. Chen, and Q. Shao, "Exploring the EM-wave diffusion capabilities of axicon coding metasurfaces for stealth applications," *Optics Express*, Vol. 31, No. 23, 37 495–37 506, 2023.

[25] Paquay, M., J.-C. Iriarte, I. Ederra, R. Gonzalo, and P. de Maagt, "Thin AMC structure for radar cross-section reduction," *IEEE Transactions on Antennas and Propagation*, Vol. 55, No. 12, 3630–3638, 2007.

[26] Han, T., K. Wen, Z. Xie, and X. Yue, "An ultra-thin wideband reflection reduction metasurface based on polarization conversion," *Progress In Electromagnetics Research*, Vol. 173, 1–8, 2022.

[27] Fu, H., N. Liu, X. Sheng, and J. Li, "An optimized coding polarization conversion metasurface with a transmission window for RCS reduction," *Applied Physics A*, Vol. 131, No. 4, 283, 2025.

[28] Wang, C., H.-X. Xu, Y. Wang, S. Zhu, C. Wang, and R. Mao, "Hybrid-phase approach to achieve broadband monostatic/bistatic RCS reduction based on metasurfaces," *Journal of Physics D: Applied Physics*, Vol. 53, No. 36, 365001, 2020.

[29] Xin, H., Y. Gao, and W. Jiang, "An ultra-wideband polarization conversion metasurface with high angular stability," in *2024 IEEE 12th Asia-Pacific Conference on Antennas and Propagation (APCAP)*, 1–2, Nanjing, China, 2024.

[30] Liu, X., J. Gao, L. Xu, X. Cao, Y. Zhao, and S. Li, "A coding diffuse metasurface for RCS reduction," *IEEE Antennas and Wireless Propagation Letters*, Vol. 16, 724–727, 2016.

[31] Han, X., H. Xu, Y. Chang, M. Lin, Z. Wenyuan, X. Wu, and X. Wei, "Multiple diffuse coding metasurface of independent polarization for RCS reduction," *IEEE Access*, Vol. 8, 162 313–162 321, 2020.

[32] Shan, H., K. Jiang, J. Xing, and T. Jiang, "BPSO and staggered triangle layout optimization for wideband RCS reduction of pixelate checkerboard metasurface," *IEEE Transactions on Microwave Theory and Techniques*, Vol. 70, No. 7, 3406–3414, 2022.

[33] Pan, Y., J. Dong, H. Luo, M. Wang, and C. Xiao, "Phase cancellation-assisted BGWO method for advanced design of ultrawideband RCS reduction metasurface," *IEEE Transactions on Microwave Theory and Techniques*, Vol. 73, No. 10, 7351–7362, 2025.

[34] Ullah, M. U., T. A. Latef, M. Othman, Y. Yamada, A. Abdrabou, T. F. T. M. N. Izam, K. A. Noordin, H. Mokhlis, K. Kamardin, and K. Dimyati, "Advanced 1-bit algorithmic approaches to PB phase metasurface optimization for radar cross-section reduction," *Ain Shams Engineering Journal*, Vol. 16, No. 8, 103466, 2025.

[35] Khan, H. A., J. Zhang, S. Luo, and Y. Wang, "A single-layer checkerboard metasurface based on reconfigurable polarization converter for dual-mode RCS reduction," *IEEE Antennas and Wireless Propagation Letters*, Vol. 24, No. 7, 2029–2033, 2025.

[36] Zhang, G., A. Wang, W. Wang, S. Sui, Y. Han, X. Fu, C. Ding, J. Wang, J. Wang, Y. Meng, and Y. Zhang, "The coding metasurface combined absorption and phase cancellation for 20 dB broadband RCS reduction," *Applied Physics A*, Vol. 131, No. 8, 642, 2025.

[37] Balanis, C. A., *Antenna Theory: Analysis and Design*, 3rd ed., John Wiley & Sons, Hoboken, NJ, USA, 2005.

[38] Yang, Z., N. Kou, S. Yu, F. Long, L. Yuan, Z. Ding, and Z. Zhang, "Reconfigurable multifunction polarization converter integrated with PIN diode," *IEEE Microwave and Wireless Components Letters*, Vol. 31, No. 6, 557–560, 2021.

[39] Zhu, S., F. Yuan, K. Hu, T. Pi, X. Zhu, and C. Li, "Design of bistatic radar cross section reduction metasurface based on convolutional neural networks," *Acta Physica Sinica*, Vol. 74, No. 10, 107802, 2025.